GEOFLUIDS

Geofluids (2015) 15, 139–160 doi: 10.1111/gfl.12111

Deep fluid circulation within crystalline basement rocks and the role of hydrologic windows in the formation of the Truth or Consequences, New Mexico low-temperature geothermal system

J. PEPIN[1], M. PERSON[1], F. PHILLIPS[1], S. KELLEY[2], S. TIMMONS[3], L. OWENS[4], J. WITCHER[5] AND C. GABLE[6]

[1]*Department of Earth & Environmental Science, New Mexico Institute of Mining and Technology, Socorro, NM, USA;* [2]*New Mexico Bureau of Geology and Mineral Resources, Socorro, NM, USA;* [3]*Aquifer Mapping Program, New Mexico Bureau of Geology and Mineral Resources, Socorro, NM, USA;* [4]*Ormat Technologies, Inc., Reno, NV, USA;* [5]*Witcher and Associates, Las Cruces, NM, USA;* [6]*EES-16 Los Alamos National Labs, Los Alamos, NM, USA*

ABSTRACT

Hot springs can occur in amagmatic settings, but the mechanisms of heating are often obscure. We have investigated the origin of the Truth or Consequences, New Mexico low-temperature (approximately 41°C) hot springs in the southern Rio Grande Rift. We tested two hypotheses that could account for this amagmatic geothermal anomaly: lateral forced convection in a gently dipping carbonate aquifer and circulation through high-permeability crystalline basement rocks to depths of 8 km that is then focused through an overlying faulted hydrologic window. These hypotheses were tested using a regional two-dimensional hydrothermal model. Model parameters were constrained by calibrating to measured temperatures, specific discharge rates, and groundwater residence times. We collected 16 temperature profiles, 11 geochemistry samples, and 6 carbon-14 samples within the study area. The geothermal waters are Na^+/Cl^--dominated and have apparent groundwater ages ranging from 5500 to 11 500 years. Hot-spring geochemistry is consistent with water/rock interaction in a silicate geothermal reservoir, rather than a carbonate system. Peclet number analysis of temperature profiles suggests that specific discharge rates beneath Truth or Consequences range from 2 to 4 m $year^{-1}$. Geothermometry indicates maximum reservoir temperatures are around 170°C. Observed measurements were reasonably reproduced using the deep circulation permeable-basement modeling scenario (10^{-12} m^2) but not the lateral forced-convection carbonate-aquifer scenario. Focused geothermal discharge is the result of localized faulting, which has created a hydrologic window through a regional confining unit. In tectonically active areas, such as the Rio Grande Rift, deep groundwater circulation within fractured crystalline basement may play a more prominent role in the formation of geothermal systems than has generally been acknowledged.

Key words: geochemistry, geothermal, hydrologic windows, numerical modeling, permeability

Received 8 February 2014; accepted 28 August 2014

Corresponding author: Jeff Pepin, Earth & Environmental Science,New Mexico Institute of Mining and Technology, Department of Earth and Environmental Science, 801 Leroy Place, Socorro, NM 87801, USA. Email: jpepin@nmt.edu. Tel: +1 575 835 5634. Fax: +1 575 835 6436.

Geofluids (2015) **15**, 139–160

INTRODUCTION

Interest in constraining crustal permeability has grown over the last 15 years (Ingebritsen & Manning 1999, 2010; Manning & Ingebritsen 1999; Shmonov *et al.* 2003; Stober & Bucher 2007). This parameter plays a key role in understanding the genesis of ore deposits (Raffensperger & Garven 1995), contact metamorphism (Gerdes *et al.* 1995), and metasomatism (Fritz *et al.* 2006). Crustal permeability is widely believed to decay with depth due to mechanical loading and fluid-rock geochemical reactions. Manning & Ingebritsen (1999) used geothermal and metamorphic data to suggest that crustal permeability decreases from 10^{-12} to 10^{-16} m^2 at 1 km depth to 10^{-15}

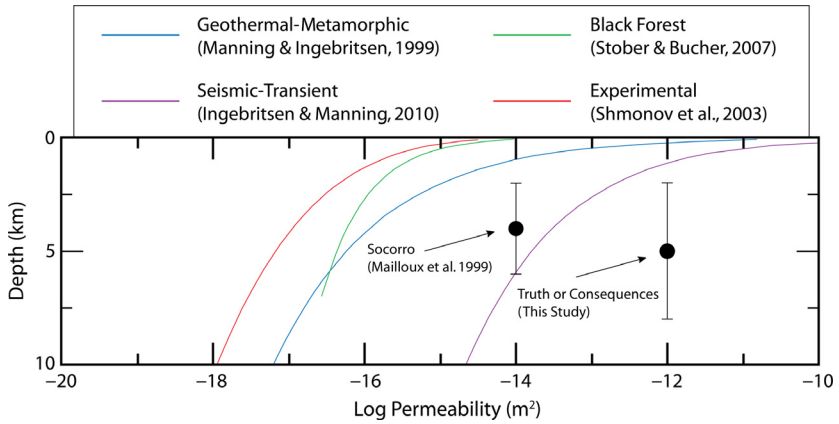

Fig. 1. Crustal permeability verses depth relationships from previous investigations that provide a range of crustal permeabilities of 10^{-18} to 10^{-10} for depths <10 km. Crystalline basement permeabilities within the Rio Grande Rift are also indicated (black circles) and are high in comparison. This suggests large fault structures and significant fracture networks have substantially increased the permeability of crystalline basement rocks in this region of New Mexico above global averages (after Ingebritsen & Manning 2010).

to 10^{-18} m^2 at 10 km depth (Fig. 1) (Ingebritsen & Manning 1999, 2010; Manning & Ingebritsen 1999; Shmonov *et al.* 2003; Stober & Bucher 2007). Independent results from various studies throughout the world provide a range for crustal permeabilities of $10^{-16.6}$ m^2 all the way up to $10^{-7.3}$ m^2 for depths <10 km (See studies in Ingebritsen & Manning 2010). These studies indicate that crustal permeabilities may vary by orders of magnitude across various geological settings at any given depth. In 2010, Ingebritsen and Manning argued that permeability has a relatively high variance while maintaining clear depth dependence for depths <10 km (Fig. 1). Deviation from this depth dependence may be due to time-dependent permeability changes as a result of tectonism and seismicity (Rojstaczer & Wolf 1992; Ingebritsen & Manning 2010).

Previous numerical modeling efforts focusing on the Rio Grande Rift suggest that crystalline basement permeability is relatively elevated (approximately 10^{-14} m^2), allowing for deep groundwater circulation (2–6 km) (Barroll & Reiter 1990; Mailloux *et al.* 1999). This permeability value is within the crustal scale permeability range determined by the aforementioned synthesis studies, although it marked a new upper limit for crystalline basement permeability along the Rio Grande Rift. In many instances, fault-block rotation, erosion, lithological variations, and emplacement of Cenozoic dikes can provide gaps or 'hydrologic windows' through overlying low-permeability Paleozoic to Cenozoic confining units, allowing pore water from the crystalline basement to discharge. In areas where crustal permeability is relatively high, the rapid rise of groundwater through hydrologic windows is probably responsible for the development of several low-temperature geothermal systems in the Rio Grande Rift (Witcher 1988; Barroll & Reiter 1990; Mailloux *et al.* 1999).

Between October 2012 and October 2013, we collected temperature, geochemical, and isotopic data to assess circulation patterns within the Truth or Consequences (T or C) hot-springs district. We also developed a cross-sectional hydrothermal model to investigate groundwater circulation patterns that formed the Truth or Consequences heat-flow anomaly (approximately 41°C at depths <54 m). Approximately 13 megawatts of heat are discharged by 0.1 m^3 sec^{-1} of geothermal water at Truth or Consequences (Theis *et al.* 1941). The majority of the geothermal groundwater ascends under the town's historic hot-springs district (referred to herein as the hot-springs district) and then flows laterally through a shallow alluvial aquifer before discharging into the Rio Grande.

The goal of this study is to determine the groundwater circulation patterns and subsurface permeability structure responsible for generating the geothermal conditions within the hot-springs district. Our analysis is intended to be broadly relevant to regions with relatively permeable fractured crystalline basement rocks and low-temperature geothermal anomalies. We tested two hypotheses using a two-dimensional numerical model (Fig. 2). The first considers relatively deep (>5 km) groundwater circulation within permeable crystalline basement rocks. Highly fractured limestone crops out locally in Truth or Consequences, indicating large fault networks are present and could foster deep groundwater circulation by greatly increasing the permeability of the subsurface. The second hypothesis is based on inferences presented in previous studies investigating the Truth or Consequences geothermal anomaly and assumes that transmission of geothermally heated water is primarily through the permeable carbonate aquifers that overly the crystalline basement rocks (Powell 1929; Theis *et al.* 1941; Wells & Granzow 1981). These carbonate layers are laterally continuous and occur at depths of about 2.7 km approximately 15 km north of Truth or Consequences.

We constrained sediment and crystalline basement permeability by reproducing hot-springs district temperature profiles and ^{14}C residence time data. A Peclet number analysis provided estimates of vertical specific discharge rates constrained by temperature profiles logged as part of this study. We compared the discharge rates from the Peclet number analysis to simulated vertical specific

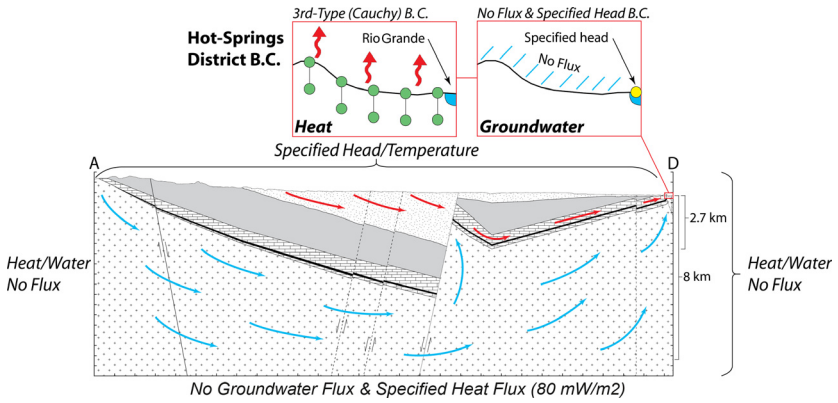

Fig. 2. Boundary conditions used in our two-dimensional hydrothermal model and a schematic diagram showing the two groundwater flow hypotheses evaluated as part of this study. Boundary conditions are shown for both heat transport and groundwater flow. The inset portrays a closeup of the boundary conditions applied to the hot-springs district. The basement-circulation hypothesis (blue arrows) involves deep circulation of groundwater within highly fractured crystalline basement rocks. Groundwater discharges where hydrologic windows exist in overlying confining units, such as the Percha Shale (black). The shallow-circulation hypothesis (red arrows) considers shallow groundwater circulation through the carbonate Magdalena Group.

discharge rates from the two-dimensional model. We also conducted a geochemical analysis of the geothermal waters, comparing geochemistry results to those of other geothermal systems of similar temperature, including New Mexico's Socorro geothermal system and the carbonate-hosted Etruscan Swell of Italy. We compared the temperatures determined by silica and cation geothermometry to simulated maximum temperatures experienced by water particles discharging in the hot-springs district. Finally, we compared our model-derived permeability estimates to those found elsewhere in the Rio Grande Rift and internationally.

Hydrogeologic setting

The Rio Grande Rift is an active 100–300 km wide, north-trending zone of crustal extension that cuts through central New Mexico (Seager & Morgan 1979; Morgan *et al.* 1986; Baldridge *et al.* 1995). The town of Truth or Consequences (formerly known as Hot Springs) is located on the banks of the Rio Grande in south-central New Mexico at the southern terminus of the Engle sub-Basin within the Rio Grande Rift (Fig. 3). The location of the geothermal system at Truth or Consequences is controlled, in part, by geologic structures that formed during three major tectonic events that affected New Mexico and the southwestern United States.

First, folds and thrust faults with a northwest-striking trend and strike-slip faults with a north-northeast-striking trend formed in the vicinity of Truth or Consequences during northeast-southwest directed compressional Laramide deformation between 75 to 45 million years ago (Seager & Mack 2003; Harrison & Cather 2004). One of the folds, a northwest-trending overturned syncline, and at least one low-angle fault, is preserved in a limestone outcrop at the northern edge of the hot-springs district. This faulted, overturned syncline is an important structure facilitating discharge of groundwater migrating southward out of the Engle Basin toward the surface (Fig. 4). Local faulting associated with this overturned syncline has created a hydrologic window in the Percha Shale that otherwise confines flow in the crystalline basement. This gap allows geothermal waters to surface in Truth or Consequences. Laramide compression was followed by voluminous eruptions in the Mogollon-Datil volcanic field starting about 37 million years ago (Harrison *et al.* 1993). Volcanic units from eruptions in the San Mateo Mountains cover the highest elevations of the Sierra Cuchillo and are buried in the Engle Basin. The third major tectonic event that shaped the landscape is Rio Grande Rift extension that began about 36 million years ago and peaked 16–5 million years ago (Kelley & Chapin 1997; Seager & Mack 2003). This event caused the uplift of the Caballo Mountains to the east and the Mud Springs Mountains, the Sierra Cuchillo, and the San Mateo Mountains to the west and northwest (Fig. 3A). Material eroded from the rising rift flank uplifts filled the Engle Basin with as much as 2.7 km of sediment (Lozinsky 1987).

Mean annual air temperature and annual precipitation are 16.5°C and 25.2 cm $year^{-1}$, respectively. Potential evapotranspiration is 84 cm $year^{-1}$ as estimated by the temperature-based Thornthwaite equation and greatly exceeds precipitation (Dingman 2002). Regional precipitation and water-table patterns indicate that the principal source of recharge to the geothermal system is probably from the Sierra Cuchillo and San Mateo Mountains to the northwest (Fig. 5). Enhanced fracture permeability in the recharge area is suggested by collapse structures associated with seven calderas identified in the San Mateo Mountains (Ferguson *et al.* 2012). We estimated recharge for the

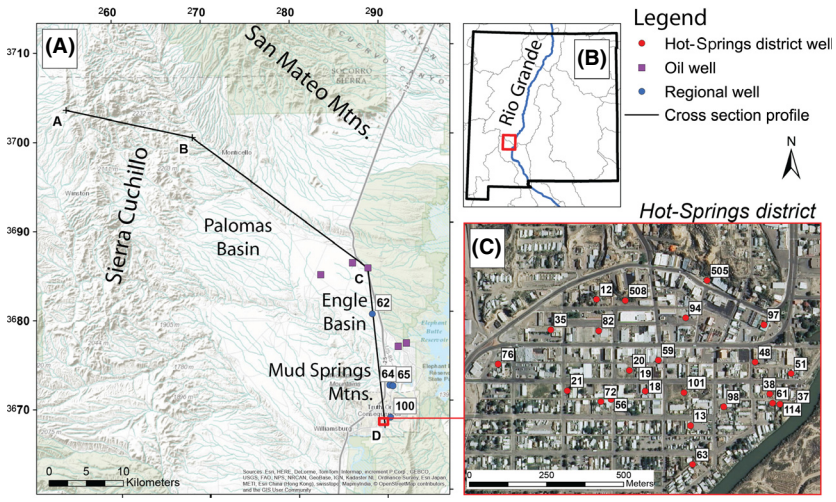

Fig. 3. Basemap (A) showing surface water drainages (light blue lines) and the location of the study area in south-central New Mexico (B). The presumed recharge area of the Sierra Cuchillo and San Mateo Mountains north of Truth or Consequences is also indicated for reference. The orientation of the geologic cross section and two-dimensional hydrothermal model is shown in black (A–B–C–D) in addition to the locations of wells discussed in this paper. The inset of the hot-springs district (C) shows geothermal well locations. The Rio Grande can also be seen in the lower right corner of this inset. The delineated areas on the New Mexico state map (B) are major drainage basins. Regional map coordinate datum is UTM NAD83 Zone 13.

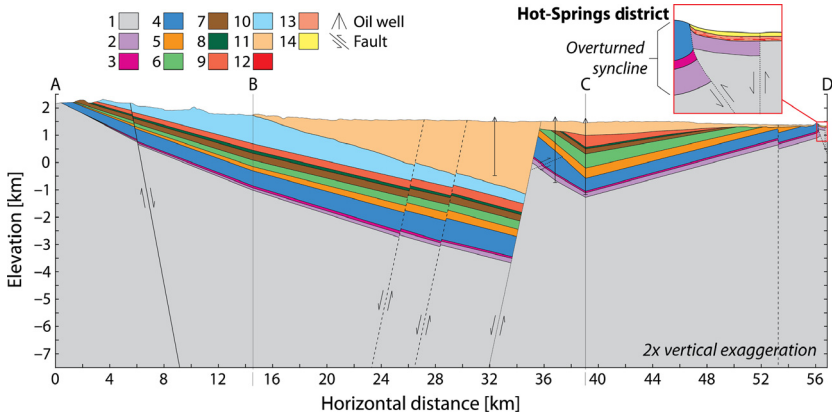

Fig. 4. Geologic cross section depicting the stratigraphic units used in our two-dimensional hydrothermal model. Additional information about model parameters is provided in Table 1. The color legend of this figure corresponds to the hydrostratigraphic units and descriptions in Table 3. The cross section was constructed by utilizing oil-well data, an east-west regional cross section (Lozinsky 1987), gravity data (Gilmer *et al.* 1986) and surface geologic maps (Harrison *et al.* 1993; Harrison & Cather 2004).

watershed using the Maxey-Eakin method, which assumes the fraction of precipitation available for subsurface recharge increases directly with precipitation. The empirical scaling coefficients used in this study are those utilized by Anderholm (2001) to estimate mountain-front recharge from the Sandia Mountains east of Albuquerque, NM. We estimate the total recharge available as between 0.1 and 0.9 m^3 sec^{-1}. The higher estimate reflects recharge over the entire watershed (Fig. 5). The lower estimate only considers recharge where Paleozoic sediments and crystalline basement rocks are exposed at the surface. The hot-springs district geothermal discharge estimate of 0.1 m^3 sec^{-1} by Theis *et al.* (1941) is consistent with the lower end of our recharge estimates. Theis *et al.* (1941) calculated this value by coupling average hot-springs district geothermal water chloride content with measurements of Rio Grande streamflow and chloride concentration above and below the hot-springs district.

Early studies of hot-springs district geothermal waters proposed magmatic heat sources (Powell 1929; Theis *et al.* 1941; Wells & Granzow 1981). However, the youngest magmatism documented near Truth or Consequences is approximately 5 million years old in the Mud Springs Mountains to the northwest (Dunbar 2005). Conceptual numerical models presented by Furlong *et al.* (1991) suggest that heat from this magmatism dissipated within <1 million years. Furthermore, swarms of microearthquakes, characteristic of magmatic activity, have not been detected beneath the study area (NMT/IRIS-PASSCAL Data Center). It is therefore unlikely that magmatic heating is involved in this geothermal system.

Previous studies (e.g., Theis *et al.* 1941) also hypothesized that circulation of the geothermal waters was primarily confined to the Magdalena Group carbonates (Fig. 2). Highly fractured limestone outcrops in the vicinity of the hot-springs district suggest permeability may be relatively high in the subsurface. The Magdalena Group carbonates dip to the north and are buried to a maximum depth of about 2.7 km, where groundwater could be heated to approximately 110°C, assuming a conductive geothermal gradient of 40°C km^{-1} (Reiter *et al.* 1986). In order for groundwater flow within the Magdalena Group carbonates to carry heat into the hot-springs district, significant lateral convective heat transfer must occur. An alternative hypothe-

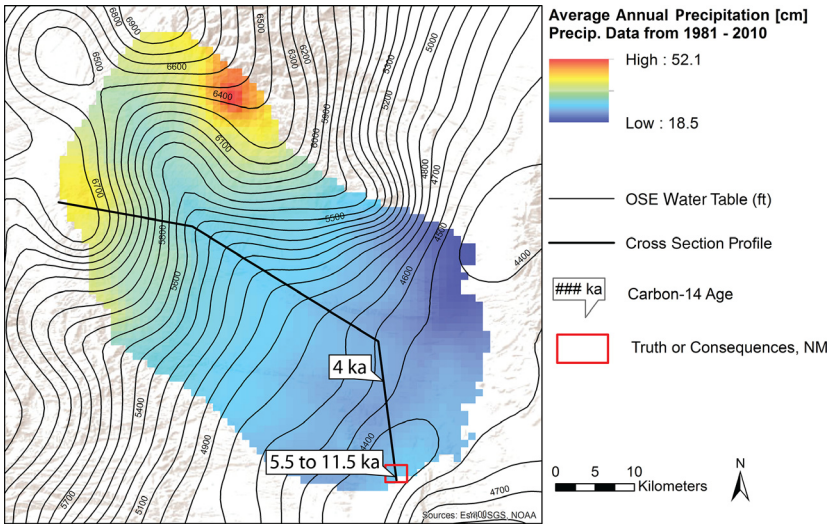

Fig. 5. Groundwater contributing area (color-shaded contours) to the hot-springs district and water table contours in relation to our two-dimensional hydrothermal model transect (bold black line). The color contours denote the spatial distribution of annual precipitation across the watershed. The black contour lines are estimated water-table elevations from the New Mexico Office of the State Engineer. Precipitation and water-table patterns suggest recharge to the hot-springs district primarily occurs in the Sierra Cuchillo and San Mateo Mountains northwest of Truth or Consequences. Apparent carbon-14 groundwater ages collected as part of this project are displayed on the basemap as well (annotated circles). Oldest groundwater ages are within the hot-springs district (precipitation data from PRISM Climate Group, Oregon State University 2012).

sis involves deep circulation through crystalline basement rocks (Fig. 2). A recently drilled 74-meter-deep well completed in fractured crystalline basement rocks yielded a permeability estimate of 2.6×10^{-10} m^2 from a preliminary specific-capacity test in June 2014; this is a very high permeability for crystalline basement rocks (this well is TC-114 in Appendix A and Fig. 3; specific-capacity test method outlined by Theis 1963). In the basement-circulation hypothesis, elevated temperatures within the hot-springs district are primarily the result of vertical convective heat transfer. Geothermal water discharges due to the localized absence of the confining Percha Shale, consistent with the hydrologic window hypothesis first proposed by Witcher in 1988.

FIELD MEASUREMENTS

Temperature profiles

We measured 16 temperature profiles to depths of 54 m. Ten of these were capped, cased wells that had not been pumped for at least 1 year (Type 1). Five profiles were from wells drilled within 2 weeks of measurement or that had their pumps removed just prior to the time of measurement but were recently active (Type 2). Data from these wells are less reliable, as the wells had recently been disturbed. One flowing artesian well was logged (Type 3).

Additional details about the wells logged are included in Appendix A, and their locations are shown in Fig. 3. Most wells displayed temperature profiles indicative of an upward flow regime (Fig. 6), as signified by negative-slope concave downward temperature profiles (Bredehoeft & Papadopulos 1965). In some instances, such curvature can be the result of horizontal flow at near steady-state conditions (Ziagos & Blackwell 1986). However, the nearly isothermal conditions at depth argue for vertical flow (Bredehoeft & Papadopulos 1965).

Groundwater residence times

We collected five carbon-14 (^{14}C) samples within the hot-springs district and one sample north of town to assess groundwater residence times. Uncorrected age precision of the samples collected is ± 50 years. All ^{14}C ages reported in this study are uncorrected, meaning their ages have not been adjusted for reservoir effects; the chemical and isotopic data necessary to confidently make corrections are not available. Plummer *et al.* (2004) used ^{14}C, ^{3}H, and CFC data to assess groundwater ages in the Middle Rio Grande Basin within the Rio Grande Rift about 250 km north of our study area. Their results suggest that geochemical corrections to radiocarbon groundwater ages may not be necessary in this region. Nonetheless, these uncorrected ages should be viewed as estimated maximum groundwater residence times. The ages acquired from our samples were used to calibrate our two-dimensional hydrothermal model.

Geochemistry

We collected 11 water samples from within the hot-springs district for geochemical analysis (Appendix B). All wells

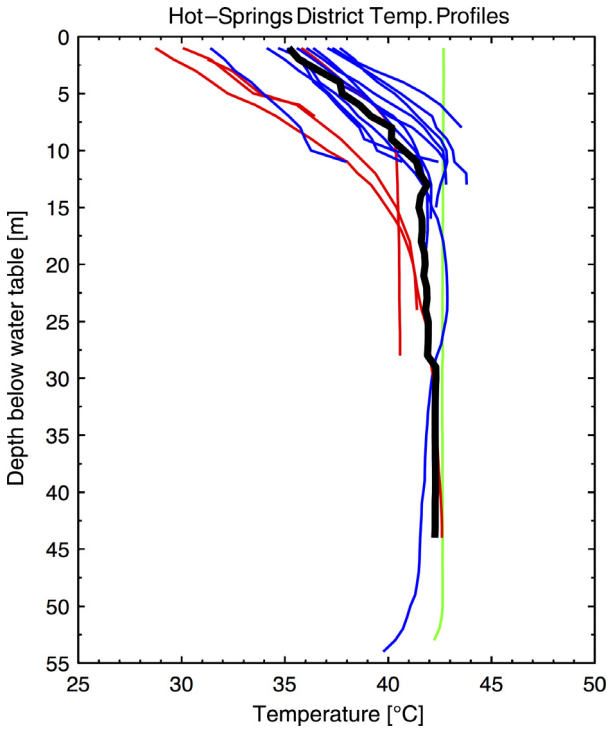

Fig. 6. Temperature-depth profiles measured within the hot-springs district during October 2012 through October 2013. The type of well the profile was measured in is indicated by its color (blue = type 1, red = type 2, green = type 3; see text in methods section for details). A calculated average profile for depths 0 to 44 m is also plotted (bold black line). The average profile was only calculated to this depth due to lack of abundant data at greater depths and was used when interpreting hydrothermal model results.

were purged with multiple borehole volumes prior to sample collection. Field parameters such as discharge temperature, pH, and specific conductance were recorded for each sample. Trace metal samples were filtered and acidified on site using a 0.45-micron filter and 10 drops of nitric acid per sample. The New Mexico Bureau of Geology and Mineral Resources chemistry laboratory analyzed the samples. Geochemical results were used in conjunction with those reported in previous studies to investigate the geochemistry and origin of the geothermal waters and to estimate geothermal reservoir temperatures using geothermometry.

THERMAL PECLET NUMBER ANALYSIS METHODS

Curvature in well temperature profiles can be used to estimate vertical flow velocities. We conducted a curve-matching exercise using the analytical solution of Bredehoeft & Papadopulos (1965) while assuming a fluid density (ρ_f) of 1000 kg m^{-3}, a fluid heat capacity (c_f) of 4180 J kg^{-1}, and bulk thermal conductivity of the sediments (λ) of 2 W (m·°C)$^{-1}$. We used the bottom-hole temperature in each well bore for T_2, while T_1 was prescribed as the water-table temperature at the top of the well; L was assigned a value of 50 m, as this is the typical depth to bedrock in the hot-springs district.

The vertical specific discharge rates from the Peclet number analysis were compared to those calculated by our two-dimensional hydrothermal model and to the geothermal discharge rate estimated by Theis *et al.* (1941).

GEOTHERMOMETRY METHODS

The chemistry of geothermal groundwater is commonly used to estimate reservoir temperatures. Constituents such as dissolved silica, calcium, potassium, and sodium are ideal for geothermometry due to their slow retrograde mineral-solute re-equilibration timescales. As geothermal groundwater ascends and cools, the temperature signature of the geothermal reservoir is preserved in the concentrations of these constituents due their slow reaction times. However, this is only true when several assumptions about the waters and their flow path are satisfied. One key assumption is that dissolution of minerals at depth is controlled by temperature-dependent chemical reactions that equilibrate at the reservoir's maximum temperature. It is also assumed that composition changes due to mixing are insignificant. Additional assumptions are described in detail by Fournier (1989) and Karingithi (2009).

Geothermometry analysis of 13 chemistry samples collected within the hot-springs district was carried out using a Microsoft Excel spreadsheet program published by Powell & Cumming (2010) entitled, 'liquid_analysis_v3_powell-cumming_2010_stanfordgw.xlsx.' Of the 13 samples analyzed, 8 were collected as part of this study, 4 were from Theis *et al.* (1941), and 1 was from Summers (1976). The composition of the samples collected as part of this study is presented in Appendix B. The Powell & Cumming (2010) spreadsheet program calculates many common geothermometers. Silica geothermometers typically represent minimum reservoir temperatures, whereas cation geothermometers provide information about maximum reservoir temperatures. This is due to the more rapid reaction rate of silica (Fournier 1989; Karingithi 2009; Powell & Cumming 2010). Some geothermometers have proven to be more consistently representative of geothermal reservoir temperatures than others; we used those suggested by Karingithi (2009) and Powell & Cumming (2010).

HYDROTHERMAL MODELING METHODS

We employed the finite element method of characteristics hydrothermal model (FEMOC) to characterize hydrology and paleohydrology within the study area (Person *et al.* 2008). The numerical approximations to the fluid flow and

heat transport equations implemented in this code were originally validated, in part, by reproducing simulations by Smith & Chapman (1983).

Groundwater flow

We solve for variable-density groundwater flow using the following stream-function-based groundwater equation (Senger & Fogg 1990):

$$\nabla_x \cdot \left[\frac{K}{|K|}\nabla_x \psi\right] = -\frac{\partial \rho r}{\partial x} \quad (1)$$

where ∇_x is the gradient operator $[L^{-1}]$, K is the hydraulic conductivity tensor $[L^1t^{-1}]$, $|K|$ is the determinant of K, ψ is the stream function $[L^2t^{-1}]$, and ρ_r is the relative density $[-]$ (defined below). The right-hand side of this equation accounts for variable-density-driven groundwater flow. While this is a steady-state groundwater flow equation, time-dependent changes in density can result in transient flow conditions.

Relative density (ρ_r) used in equation (1) is defined as:

$$\rho_r = \frac{\rho_f - \rho_o}{\rho_o} \quad (2)$$

where ρ_f is the density of groundwater at its elevated temperature and pressure $[M^1L^{-3}]$, and ρ_o is the density of water at standard conditions (10°C and atmospheric pressure) $[M^1L^{-3}]$.

Specific discharge is related to the stream function through the Cauchy–Riemann equations:

$$\frac{\partial \psi}{\partial z} = q_x \quad (3)$$

$$-\frac{\partial \psi}{\partial x} = q_z \quad (4)$$

where q_x and q_z are specific discharge $[L^1t^{-1}]$ in the x and z directions $[L^1]$, respectively.

Heat transport

Temperature can affect groundwater density in our model. FEMOC solves a conductive and convective-dispersive heat transfer equation given by:

$$[c_f \rho_f \varphi + c_s \rho_s (1-\varphi)]\frac{\partial T}{\partial t} = \nabla_x[\lambda \nabla_x T] - \bar{q}\rho_f c_f \nabla_x T \quad (5)$$

where λ is the thermal dispersion-conduction tensor $[M^1L^1t^{-3}T^{-1}]$, t is time $[t^1]$, φ is porosity $[-]$, T is temperature $[T^1]$, c_s is the specific heat capacity of the solid phase $[L^2t^{-2}T^{-1}]$, c_f is the specific heat capacity of the liquid phase $[L^2t^{-2}T^{-1}]$, $\bar{q}$ is the specific discharge vector $[L^1t^{-1}]$, ρ_f is the density of the liquid phase $[M^1L^{-3}]$, and ρ_s is the density of the solid phase $[M^1L^{-3}]$. Thermal conductivities are assumed to be isotropic, as we have used scalar quantities.

Groundwater residence time

Reverse particle tracking was used to determine simulated groundwater residence times. The particle tracking algorithm utilizes the final seepage velocity field generated by FEMOC to advect particles throughout the finite element domain (Person *et al.* 1998). Particle tracking along flow paths permitted the determination of maximum temperatures experienced by groundwater discharging in the hot-springs district.

Equations of state

Thermodynamic equations of state are used to compute the density and viscosity of groundwater at elevated temperature and pressure conditions. FEMOC uses the polynomial expressions of Batzle & Wang (1992), valid for temperatures between 10 and 350°C.

Boundary conditions

The boundary conditions assigned in our model are most consistent with field evidence. For groundwater flow, the lateral regional water-table gradient published by the New Mexico Office of the State Engineer was used to assign specified head values across the top of the model domain (Fig. 2). FEMOC uses this head gradient to determine a surface flux using the following steady-state stream function equation:

$$\frac{\partial \psi}{\partial z} = -K\frac{\partial h}{\partial x} \quad (6)$$

where K is the hydraulic conductivity $[L^1t^{-1}]$, h is hydraulic head $[L^1]$, and ψ is the stream function $[L^2t^{-1}]$. Assigned water-table elevations varied from 2143 m in the Sierra Cuchillo to 1331 m in the hot-springs district (Fig. 5). A no-flux boundary condition was assigned locally near the southern edge of the model domain within the hot-springs district. This was performed to emulate shallow lateral geothermal water flow toward the Rio Grande. At the southern terminus of the model domain, the Rio Grande was represented as a specified head node. The sides and base of the solution domain were represented as no-flux boundaries. The no-flux boundary condition on the northern end of the domain represents the watershed divide in the Sierra Cuchillo. The no-flux boundary condition on the southern end, at the Rio Grande, forces waters to rise and discharge. Water-table temperature measurements in wells on the opposite side of the Rio Grande near Truth or Consequences are cold relative to the hot-springs district. This suggests that the Rio Grande serves as a

no-flux boundary for the geothermal waters; it is also the regional topographic low point in the area.

For heat transport, a specified temperature boundary condition was assigned across most of the top of the solution domain at the water table (Fig. 2). Assigned water-table temperatures ranged from 15°C in the uplands to 24°C near the hot-springs district. A third-type or Cauchy boundary condition was assigned along the surface locally in the hot-springs district. This was performed so that near-surface temperatures were free to vary with the magnitude of convective heat transfer. This boundary condition utilizes simulated temperature gradients just below the water table and the effective thermal conductivity of the vadose zone to compute the vertical conductive heat flux across the surface. Along the base of the solution domain, we assigned a basal heat flux of 80 mW m^{-2}, which closely resembles measured heat flux values near Truth or Consequences (Sass *et al.* 1971; Sanford *et al.* 1979; Reiter *et al.* 1986). No-flux boundaries were imposed on the sides of the domain.

Initial conditions

Initial subsurface temperatures were assumed to increase linearly with depth using a 40°C km^{-1} temperature gradient that is representative of the region (Reiter *et al.* 1986). All model simulations were run for 300 000 years using a time step of 20 years to reach steady-state conditions in order to eliminate the influence of initial conditions.

Mesh configuration

The cross-sectional finite element mesh included 3904 nodes and 7493 triangular elements. We used 123 nodal columns to discretize 14 hydrostratigraphic units present in the study area. The mesh was vertically and laterally refined within the hot-springs district. The horizontal dimensions of the grid varied from 1000 m to the north to 50 m within the hot-springs district. Except for very thin hydrostratigraphic units of 10–20 m in thickness, there are 2–3 nodes per stratigraphic layer in the vertical direction. Within the unconsolidated deposits of the hot-springs district, vertical grid dimensions average about 10 m. The vertical discretization of the crystalline basement varies from 100 m to 800 m beneath the hot-springs district.

Hydrostratigraphy and simulation parameters

We constructed our northwest-southeast cross-sectional model perpendicular to the New Mexico State Engineer's published regional water-table contours (Figs 4 and 5). While no one cross section fully captures three-dimensional flow patterns, this cross section provides a reasonable estimate of groundwater flow patterns associated with the Truth or Consequences geothermal system. The stratigraphy of the cross section was constrained using oil-well data, an east-west regional cross section (Lozinsky 1987), gravity data (Gilmer *et al.* 1986), and surface geologic maps (Harrison *et al.* 1993; Harrison & Cather 2004). The hydrologic parameters assigned to each of the 14 stratigraphic units are presented in Table 1. Insufficient well-test data exist to assign locally derived hydrologic parameters. Therefore, we used representative permeability and porosity values consistent with those reported by Freeze & Cherry (1979). Thermal transport and petrophysical parameters that were assigned to all hydrostratigraphic units and held constant are presented in Table 2. Brief geologic descriptions of the hydrostratigraphic units are given in Table 3. Stratigraphic offsets caused by faults were included in the model, but discrete faults were not modeled as conduits or barriers to groundwater flow.

Table 1 Hydrologic parameters assigned to different stratigraphic units. Crystalline basement (Unit 1) and Magdalena Group (Unit 4) permeabilities are variable.

Unit	Unit name	Log(k_x) (m^2)	Anisotropy (k_x/k_z)	Porosity
1	Precambrian Granitic and Metamorphic Rocks	−19 to −11	1	0.05
2	Additional Lower Paleozoic Formations	−14	1	0.15
3	Lower Paleozoic Percha Shale, Lake Valley Formation, Kelley Limestone	−19	1	0.15
4	Pennsylvanian Magdalena Group	−13 to −11	1	0.20
5	Permian Abo Formation	−15	1	0.25
6	Permian Yeso Formation	−17	1	0.25
7	Permian San Andres Formation	−17	1	0.25
8	Cretaceous Mancos Shale & Dakota Sandstone	−17	1	0.25
9	Cretaceous Sediments	−17	1	0.25
10	Tertiary Volcanics	−16	1	0.15
11	Tertiary Palomas Formation	−12	100	0.30
12	Quaternary Sand & Gravel	−12	100	0.30
13	Quaternary Fine Sand	−12	100	0.30
14	Quaternary Clay	−17	1	0.30

Table 2 Thermal, solute transport, and physical parameters held constant for all simulations and all hydrostratigraphic units.

Symbol	Variable name	Magnitude
α_L	Longitudinal dispersivity	10 m
α_T	Transverse dispersivity	1 m
λ_f	Fluid thermal conductivity	0.58 W m^{-1} °C^{-1}
λ_r	Solid thermal conductivity	2.5 W m^{-1} °C^{-1}
ρ_s	Rock density	2600 kg m^{-3}
S_s	Specific storage	10^{-7} m^{-1}

Table 3 Brief lithologic description of each of the 14 stratigraphic units. Thickness estimates are based on oil well logs and surface outcrops (See Lozinsky 1987).

ID	Name	Thickness [m]	Description
1	Precambrian Granitic and Metamorphic Rocks		Metamorphosed volcanic rocks, sandstone, and shale deposited in an extensional basin about 1.60 to 1.65 billion years ago, later intruded by 1.4 billion year age granite.
2	Additional Lower Paleozoic Formations	0–175	Cambrian to Silurian shallow marine limestone, dolomite, shale and sandstone; includes, from oldest to youngest, Bliss Sandstone, El Paso Formation, Montoya Formation, and Fusselman Dolomite.
3	Lower Paleozoic Percha Shale, Lake Valley Formation, Kelley Limestone	0–50	The Devonian Percha Shale includes shale intercalated with thin siltstone and limestone beds. The Percha Shale grades up into the carbonates of the Mississippian Lake Valley Formation. The Percha Shale is a confining unit.
4	Pennsylvanian Magdalena Group	200–816	Fossiliferous limestone, cherty limestone, shale, dolomite, and conglomerate deposited in shallow ocean water that grade up into Abo Formation.
5	Permian Abo Formation	10–397	River floodplain mudstone and siltstone, sinuous channel sandstones, and rare carbonate lake deposits. This formation is generally a confining unit.
6	Permian Yeso Formation	10–533	Predominantely sandstone and gypsum with layers of limestone, siltstone, and shale.
7	Permian San Andres Formation	20–231	Fossiliferous marine limestone, shale and fine-grained sandstone.
8	Cretaceous Mancos Shale & Dakota Sandstone	0–50	Fluvial sandstone, shale, and conglomerate of the Dakota grades up into two tongues of Mancos Shale. The Mancos Shale tongues act as confining units.
9	Cretaceous Sediments	0–435	Sandstone, shale, and conglomerate of the marginal marine Gallup Sandstone and fluvial Crevasse Canyon Formation.
10	Tertiary Volcanics	375–1020	Lava flows, ash flow tuffs, debris and stream deposits that formed during voluminous eruptions in the Mogollon-Datil volcanic field. Fracturing has increased this unit's permeability.
11	Tertiary Palomas Formation	10–2000	Weakly to moderately cemented sandstones, conglomerates, and siltstones deposited in the Engle Basin to the north of Truth or Consequences during Rio Grande rift extension.
12	Quaternary Sand & Gravel	0–20	These Quaternary alluvial sediments deposited locally in Truth or Consequences are a mixture of alluvial fan and fluvial sediments.
13	Quaternary Fine Sand	0–30	Quaternary fluvial sediments that contain clay lenses. Units 13 and 14 combine to form a leaky confining unit in the hot-springs district.
14	Quaternary Clay	0–7	Clay layers within the hot-springs district's Quarternary fine sands.

Numerical implementation

We solved the governing equations sequentially using the finite element method. The groundwater flow equation was solved using Galerkin's method with triangular elements and linear trial solutions. The heat transport equation was solved using the modified method of characteristics (MMOC). Reverse particle tracking to obtain groundwater residence times and advective ages was performed using the seepage velocity field from the last time step in each simulation.

Permeability can vary by several orders of magnitude for a given lithology. We conducted a sensitivity study and calibration procedure in which we varied the permeability of the Magdalena Group carbonates (unit 4) between 10^{-13} and 10^{-11} m^2 and that of crystalline basement (unit 1) from 10^{-19} to 10^{-11} m^2. These permeability values are within the range noted by Freeze & Cherry (1979) and Gleeson *et al.* (2011) for these lithologies. Forty-one simulations were run to complete the trial and error calibration process. We present model output from 7 of these simulations below.

RESULTS

Peclet number analysis results

Curvature in nearly all of the temperature profiles collected within the hot-springs district is evidence of upward groundwater migration (Fig. 6). Specific discharge was determined for 10 of these wells using Peclet number analysis. Our best-fit Peclet number results indicate vertical specific discharge rates ranging from 2 to 4 m year^{-1} beneath Truth or Consequences (Fig. 7). Theis *et al.* (1941) estimated geothermal discharge from the hot-springs district to be 0.1 m^3 sec^{-1}. Most of the geothermal waters discharge in the hot-springs district, which comprises an area of 750 m by 750 m. Dividing the

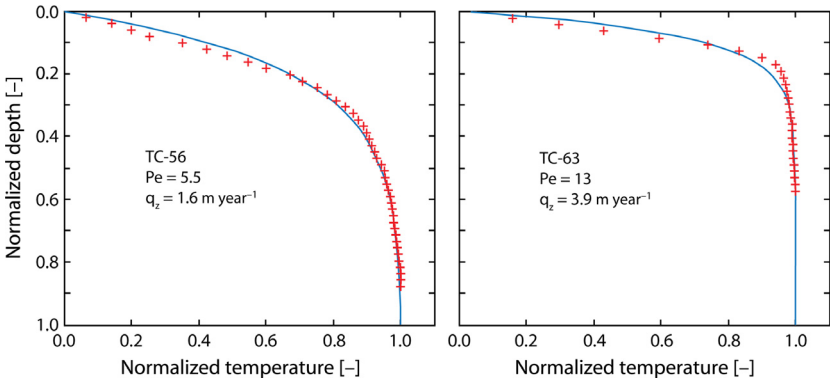

Fig. 7. Peclet number analysis results from two representative wells. Our best-fit curve-matched results indicate vertical specific discharge rates ranging from 2 to 4 m year^{-1} beneath the hot-springs district. See Fig. 3C for well locations.

0.1 m^3 sec^{-1} discharge estimate by the approximate area of the hot-springs district yields a vertical specific discharge rate of around 6 m year^{-1}. Considering the typical accuracy of Peclet number analysis and the uncertainty associated with the discharge approximation by Theis *et al.* (1941), the calculated specific discharge estimates are in reasonable agreement.

Groundwater residence time results

Uncorrected carbon-14 groundwater ages within the hot-springs district ranged between 5490 and 11 480 years. A ^{14}C sample collected approximately 14 km north of town provided a younger uncorrected age of 4040 years. Shallow groundwater within alluvial deposits will typically yield ages on the order of hundreds of years (Weissmann *et al.* 2002). The ages collected in Truth or Consequences support a deep flow path for the geothermal waters.

Geothermometry results

Geothermometry results are summarized in Table 4. Silica geothermometers and the K/Mg geothermometer provide information about near-discharge area conditions, as they react more rapidly than other geothermometers (Fournier 1989; Karingithi 2009; Powell & Cumming 2010). Na/K and Na-K-Ca cation geothermometers preserve a longer record of the flow history due to slower retrograde equilibration rates. Consequently, they typically reflect more distant and deeper reservoir temperatures.

The silica geothermometers and K/Mg geothermometer suggest temperatures ranging from 63 to 102°C. The slower-to-equilibrate cation geothermometers indicate temperatures ranging from 158 to 207°C. When Na-K-Ca geothermometry indicates reservoir temperatures are below 180°C, a magnesium correction is sometimes applied. The magnesium-corrected Na-K-Ca geothermometer yields reservoir temperatures ranging from 100 to 125°C. The value of $[\log_{10}(\sqrt{Ca}Na^{-1}) + 2.06]$ is slightly positive at 0.3 for all of the samples analyzed. This suggests the most appropriate cation geothermometer for determining deep reservoir temperatures may be the Na-K-Ca geothermometer, which yields temperatures ranging from 122 to 183°C, or the Na-K-Ca magnesium-corrected geothermometer, which ranges from 100 to 125°C (Karingithi 2009). Averaging the slower-to-equilibrate cation geothermometers indicates maximum reservoir temperatures around 167°C. Dividing this value by the local geothermal gradient (40°C km^{-1}; Reiter *et al.* 1986) implies geothermal groundwater circulation to depths around 4 km.

Geothermometry temperatures should be applied cautiously. Groundwater at temperatures in excess of 180°C is generally in equilibrium with silica (Karingithi 2009). Cation geothermometers, including the Na-K-Ca magnesium-corrected geothermometer, average 167°C and imply that silica may have not reached equilibrium in the reservoir.

Table 4 Summary of silica and cation geothermometry results. Silica geothermometers represent a minimum reservoir temperature while cation geothermometers provide information about maximum reservoir temperatures. Estimated depths were calculated by dividing the mean geothermometer temperature by the geothermal gradient of 40°C km^{-1} (Reiter *et al.* 1986).

Type	Geothermometer	Source	Mean (°C)	Min. (°C)	Max. (°C)	Range (°C)	Est. Depth [km]
Silica	Chalcedony cond.	Fournier & Potter (1982)	63	51	77	26	1.6
	Quartz cond.	Fournier & Potter (1982)	94	83	107	24	2.4
	Quartz adiabatic	Fournier (1981)	96	85	107	21	2.4
Cation	Na-K-Ca	Fournier (1981)	158	122	183	61	4.0
	Na-K-Ca Mg corr	Fournier (1981)	113	100	125	25	2.8
	Na/K	Fournier (1979)	190	168	208	39	4.7
	Na/K	Giggenbach (1988)	207	186	223	37	5.2
	K/Mg	Giggenbach (1986)	102	93	111	18	2.6

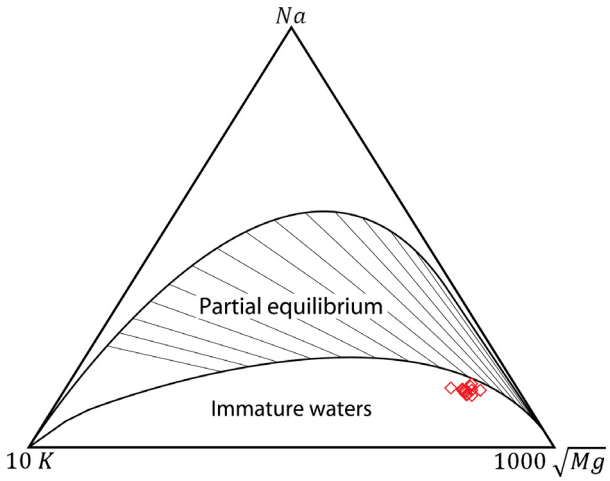

Fig. 8. Giggenbach (1991) plot of the geothermal waters collected in the hot-springs district. This plot classifies them as 'immature waters,' implying that cation geothermometry results may not be representative of geothermal reservoir tempertures at depth due to mixing or lack of equilibration.

Further, a Giggenbach plot classifies the hot-springs district waters as immature, signifying they may not be representative of geothermal reservoir conditions (Fig. 8). In general, cation geothermometry temperature uncertainties are typically about 20°C (Fournier 1989).

Groundwater geochemistry results

Geochemical data from this study, Theis *et al.* (1941) and Summers (1976), are summarized on a Piper diagram in Fig. 9. The hot-springs district waters have total dissolved solids (TDS) contents averaging about 2600 ppm, which is fairly high for the region. Shallow nonthermal waters typically have TDS concentrations of <500 ppm. The analyses of the geothermal waters are very similar, such that most of them overlie each other in Fig. 9. The Na^+/Cl^- composition of the hot-springs district geothermal waters is characteristic of high-to-moderate temperature water in crystalline basement rocks (Kühn 2004; Stober & Bucher 2007; Bucher & Stober 2010). The Na^+ is known to be derived from fluid-rock alteration reactions at relatively high temperatures, and the Cl^- is released from fluid inclusions as the rock is altered (Ellis & Mahon 1964, 1967).

Two analyses of Rio Grande streamflow are plotted in Fig. 9 for comparison. The samples were collected 7 months apart from the Rio Grande just north of Truth or Consequences, below Elephant Butte Dam. The Rio Grande has a mixed Na^+/Ca^{2+} cation composition, anions dominated by HCO_3^- and SO_4^{2-}, and is relatively dilute. Several nearby (within 16 km), mildly geothermal waters (20 to 30°C) are similar to the hot-springs district geothermal waters, but have higher concentrations of Ca^{2+} and SO_4^{2-}. Some of these waters have a composition intermediate between the hot-springs district groundwater and the Rio Grande, suggesting mixing of dilute shallow water with geothermally derived water.

We further explore the possibility of mixing by plotting sodium and trace element concentrations closely associated with typical geothermal waters against the concentration of chloride. Throughout the Great Basin, geothermal waters tend to show a close correlation between reservoir temperature and chloride concentrations. Geothermal waters from the Basin and Range typically have elevated boron and lithium concentrations that also correlate with chloride (Arehart *et al.* 2003). Covariation with the chloride concentration thus supports a mixing hypothesis (Fig. 10). The mildly geothermal waters in some cases do not follow the general trend; temperatures fall below the trend, and one sample has notably high boron content (indicated with an arrow in Fig. 10). The elevated boron content of marine shales makes them a common source of boron in groundwater (Harder 1959; Walker 1975), so a likely source is the marine Percha Shale, thought to have been removed from the hot-springs district by faulting. The covariation of the remaining samples with chloride strongly supports the hypothesis that Truth or Consequences is supplied by a geothermal aquifer of quite homogeneous composition that is locally diluted by cooler shallow waters. It also provides further evidence that the geothermometry results may not accurately represent geothermal reservoir conditions due to mixing during ascent.

Groundwater residing in carbonate rocks at high temperatures would be expected to exhibit a $Ca^{2+}/HCO_3^-/SO_4^{2+}$ composition (Chiodini *et al.* 1995), similar to those from the 'Etruscan Swell' area of Italy. However, the geochemical composition of groundwater from the carbonate system is quite distinct from the Truth or Consequences waters (Fig. 9).

The Socorro, New Mexico geothermal system (Owens 2013), is thought to result from deep circulation within highly fractured crystalline rocks (Barroll & Reiter 1990; Mailloux *et al.* 1999). Average Socorro water temperatures are slightly lower than the hot-springs district waters, averaging about 36°C, and their TDS content is a little lower (approximately 2100 ppm), but their overall chemistry is similar to the hot-springs district samples. This suggests the Truth or Consequences and Socorro groundwaters circulate primarily in rocks of similar composition, most likely igneous and metamorphic basement rocks.

Two-dimensional hydrothermal modeling results

Here, we present 7 representative hydrothermal model results that serve to evaluate the groundwater circulation hypotheses mentioned in the introduction and depicted in Fig. 2. The first hypothesis involves highly permeable crystalline basement rocks and the relatively rapid ascent of

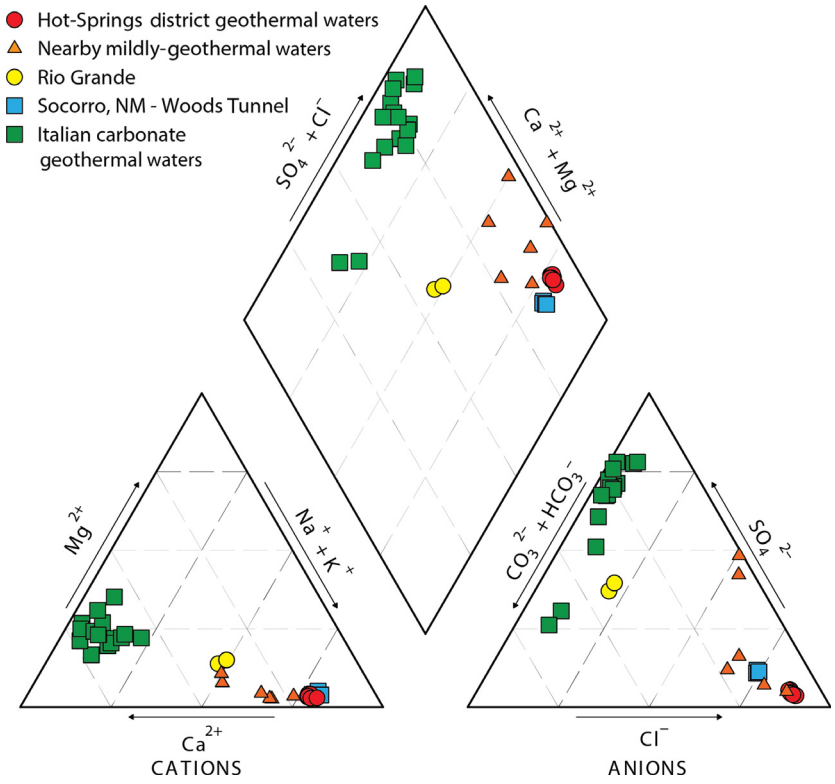

Fig. 9. Piper diagram summarizing geochemical analyses discussed in this paper. The geothermal waters from the hot-springs district are shown with red circles. Mildly geothermal waters in the vicinity (within 16 km) of the hot-springs district are plotted as orange triangles. Two samples of Rio Grande surface waters collected upstream of Truth or Consequences are shown using yellow circles. Data from a low-temperature carbonate geothermal reservoir in the Etruscan Swell of Italy (Chiodini *et al.* 1995) are shown with green squares. Data from the Woods Tunnel slim hole from the Socorro, New Mexico geothermal system are shown by blue squares (Owens 2013). Truth or Consequences waters have a Na^+/Cl^- signature characteristic of geothermal waters derived from igneous and metamorphic rocks.

geothermal waters through a hydrologic window in a regional confining unit (i.e., the Percha Shale) and will be referred to as the basement-circulation hypothesis. The second hypothesis considers shallow circulation through the permeable Magdalena Group carbonates and will be referred to as the shallow-circulation hypothesis. The goal of each scenario was to try to reproduce the temperature profiles, vertical specific discharge rates, and carbon-14 groundwater ages measured or estimated.

We tested the deep-circulation hypothesis by varying the permeability of crystalline basement rocks from 10^{-14} to 10^{-11} m^2 (Fig. 11D–G). This allowed circulation to depths of around 8 km. Geothermal waters discharge in the hot-springs district and to a lesser degree in the center of the model domain, near the Mud Springs Fault. In both of these areas, hydrologic windows are present in overlying confining units due to faulting. The regional temperature distribution for all deep-circulation scenarios is the result of a forced-convection heat-flow regime, with the exception of the lowest basement permeability case (10^{-14} m^2), which is conduction-dominated (Fig. 11D–G; Smith & Chapman 1983). Regional forced convection results in the redistribution of heat toward the topographically low southern side of the model domain. The warmest simulated temperatures are on the south side of the hot-springs district (Fig. 12D–G), which is somewhat inconsistent with field observations, as hottest measured temperatures occur in the center of the district, approximately 300 m north of our warmest simulated temperatures. We extracted temperature profiles from the warm region in the model for comparison to locally measured temperature profiles. Comparing a representative average of these simulated profiles to the average measured profile from Fig. 6 shows that assigned basement permeabilities of 10^{-13} and 10^{-12} m^2 produce the best agreement with observed hot-springs district temperatures (Fig. 13D, Table 5). Basement permeabilities outside the 10^{-13} to 10^{-12} m^2 range resulted in groundwater temperatures that were too low. The net cooling effect with high permeabilities, as evidenced in our 10^{-11} m^2 scenario, is consistent with patterns observed in many prior studies (e.g., Smith & Chapman 1983). Specific discharge rates calculated in our Peclet number analysis and inferred from Theis *et al.* (1941) most closely matched our basement permeability

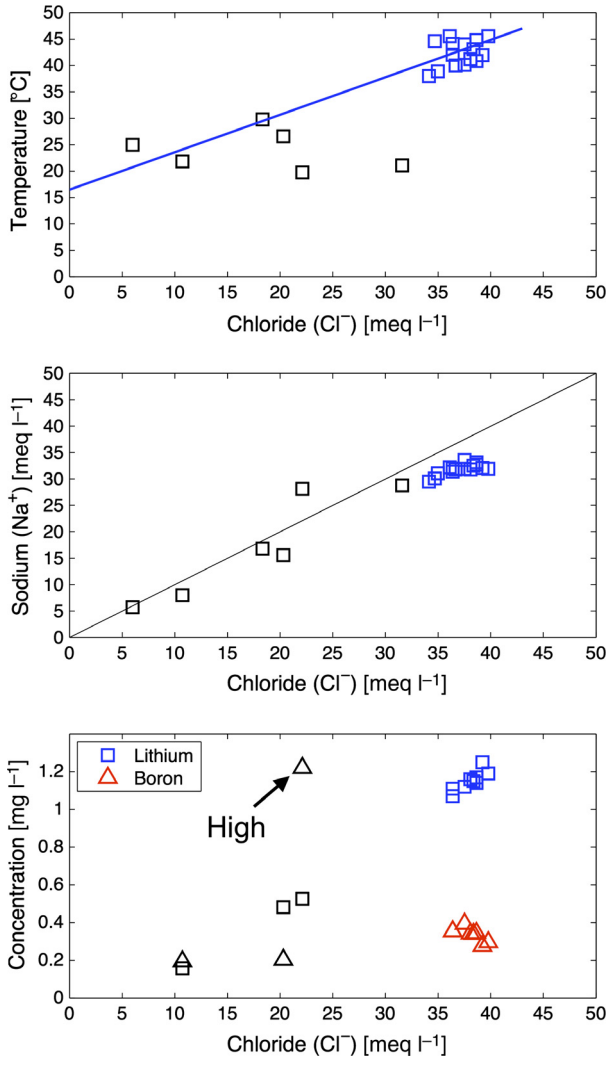

Fig. 10. Plots of groundwater temperature (top), Na^+ (middle), and B and Li^+ (bottom) against Cl^-. Mildly geothermal groundwaters near the hot-springs district (within 16 km) are shown using black squares. The blue line in the top figure connects mean annual temperature at Truth or Consequences (16.5°C) to the temperature of the geothermal waters. The black line on the middle plot is a 1:1 line. The black arrow on the bottom plot highlights a well located about 5 km north of the hot-springs district that has elevated concentrations of boron. The blue and red lines in the bottom plot are trendlines for lithium and boron data, respectively. All plots show covariation, suggesting geothermal Na^+/Cl^- waters have undergone mixing with shallow non-geothermal groundwater.

scenario of 10^{-12} m^2 (33% and −29% error, respectively). Simulated hot-springs district residence times for the basement-circulation scenarios had a wide range of 7770 years to 491 012 years (Table 5). The simulated residence times closest to carbon-14 ages were obtained when employing basement permeabilities of 10^{-11} m^2 (7% error) and 10^{-12} m^2 (167% error). Finally, comparing the maximum estimated reservoir temperatures from particle tracking to the average cation geothermometry results show best agreement with basement-permeability scenarios of 10^{-12} m^2 (28% error) and 10^{-11} m^2 (5% error). In addition to the constant permeability-with-depth scenarios presented here, we also considered a permeability decay with depth scenario for the crystalline basement rocks (not shown) using the relation presented by Manning & Ingebritsen (1999). However, this scenario resulted in near-conductive conditions due to the rapid decay of permeability and resulting shallow groundwater circulation patterns.

To test the shallow-circulation hypothesis, we set the crystalline basement permeability to 10^{-19} m^2 and varied the Magdalena Group carbonates' permeability from 10^{-13} to 10^{-11} m^2. This effectively restricts groundwater circulation to the shallow carbonate aquifer, as shown in Fig. 11A–C. Water discharging in the hot-springs district enters the system from both the primary recharge area in the north and a zone near the Mud Springs Fault in the center of our model domain. All computed shallow-circulation temperature distributions are indicative of conduction-dominated heat transport (Fig. 11A–C). Simulated hot-springs district temperature patterns are similar for these scenarios and are warmer toward the south end of the district (Fig. 12A–C). Temperature profiles extracted from this zone do not match the observed average temperature profile from the hot-springs district (Fig. 13C). Increasing the permeability of the carbonate aquifer did not result in higher regional or hot-springs district temperatures. Specific discharge calculations for these shallow-circulation scenarios were smaller than both the Theis *et al.* (1941) estimate and the Peclet number analysis results by more than 95%. Computed hot-springs district residence times also poorly matched field measurements. Finally, cation geothermometry results were not in agreement with the simulated maximum temperatures.

For both the shallow- and deep-circulation simulations, computed regional temperature profiles agree fairly well with bottom-hole temperature data measured in two oil wells located approximately 15 km north of Truth or Consequences (Fig. 13A,B). This is likely due to the fact that groundwater flow is largely horizontal in this region, and temperatures are close to conductive conditions. The reasonable agreement between simulated and observed temperatures near these wells suggests that the basal heat flux and thermal conductivities we assigned in our model are representative.

DISCUSSION & CONCLUSIONS

Numerical modeling results and geochemical interpretation strongly suggest that the Truth or Consequences geothermal system is the result of deep groundwater circulation within fractured permeable crystalline basement rocks. Faulting has made regional confining units locally discon-

Table 5 Comparison of average simulated hot-springs district (HSD) temperatures and ages to those observed. Average observed (41.1°C) and simulated temperatures have been calculated by averaging temperature profiles spanning 0–44 m. Observed carbon-14 dates collected within the HSD are interpreted as representative groundwater residence times and have been averaged (7292 years) for comparison with advective particle travel times using the steady-state flow field simulated by our cross-sectional model. All shallow circulation scenarios fail to reproduce HSD temperatures. Scenarios E and F accurately simulate temperatures. However, all other calibration parameters are better fit by scenario E, suggesting a crystalline basement permeability of 10^{-12} m^2 is most likely. The permeability assigned to the crystalline basement (PC) and Magdalena Group carbonates (Pm) are listed.

				HSD temperatures.		Particle temperatures.	
Scenario	ID	Pm log(k) (m^2)	PC log(k) (m^2)	Average (°C)	% Error	Maximum (°C)	% Error
Shallow circulation	A	−11	−19	28.2	−31	85.5	−49
(varying Pm)	B	−12	−19	29.1	−29	85.0	−49
	C	−13	−19	29.1	−29	62.5	−63
Basement circulation	D	−13	−11	33.0	−20	175.5	5
(varying PC)	E	−13	−12	40.3	−2	213.0	28
	F	−13	−13	41.3	0	241.2	44
	G	−13	−14	30.8	−25	129.1	−23

				Specific discharge			Age	
Scenario	ID	Pm log(k) [m^2]	PC log(k) [m^2]	Average (m $year^{-1}$)	% Error (1941)	% Error (Peclet)	Average (years)	% Error
Shallow circulation	A	−11	−19	0.1	−99	−97	502 802	6795
(varying Pm)	B	−12	−19	0.1	−99	−97	63 667	773
	C	−13	−19	0.1	−99	−97	498 818	6741
Basement circulation	D	−13	−11	10.1	81	237	7770	7
(varying PC)	E	−13	−12	4.0	−29	33	19 465	167
	F	−13	−13	0.6	−90	−80	128 000	1655
	G	−13	−14	0.1	−99	−97	491 012	6634

Observed Data: hot-springs district Temp. = 41.1°C; Geothermometry = 167°C.Observed Data: Spec. Discharge (1941) = 5.6 m $year^{-1}$; Spec. Discharge (Peclet) = 3.0 m $year^{-1}$; Age (Carbon-14) = 7292 years.

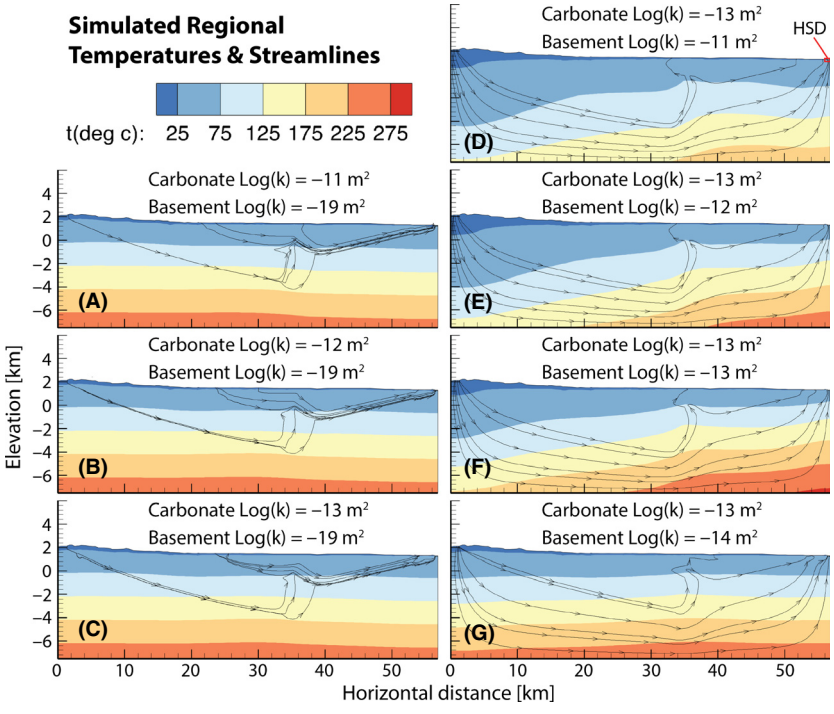

Fig. 11. Comparison of computed regional groundwater flow patterns (black lines with arrows) and temperatures for three shallow circulation scenarios (left, A–C) and four basement circulation scenarios (right, D–G). The base-10 logarithm of permeabilities used for the Magdalena Group and the crystalline basement are listed above each plot. Refer to Table 5 for simulation parameters and goodness of fit for subplots A–G. The location of the hot-springs district (HSD) is shown in graphic D. Groundwater flow directions are parallel to streamlines. Groundwater reaching the hot-springs district in the shallow circulation scenarios flows primarily through the shallow Magdalena Group. In constrast, deep circulation scenarios are characterized by geothermal waters derived predominately from crystalline basement rocks. Shallow circulation scenarios yield thermal patterns typical of a conductive thermal regime.

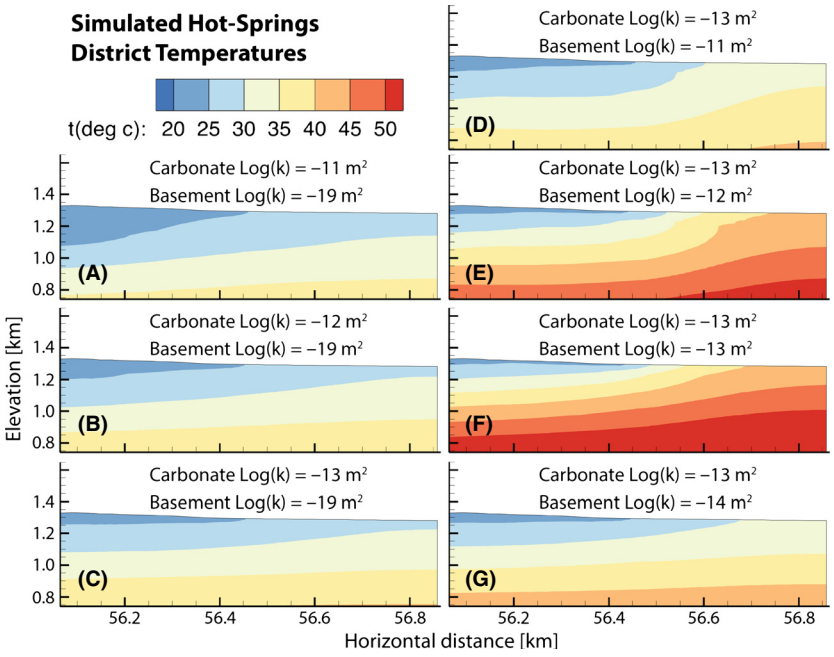

Fig. 12. Comparison of computed hot-springs district temperature patterns for three shallow circulation scenarios (left) and four basement circulation scenarios (right). Refer to Table 5 for simulation parameters and goodness of fit for subplots A–G. The relative regional location of these cross-sections is shown in Fig. 11D denoted by 'HSD'. Only two (simulations E and F) of the presented simulations reproduced average measured hot-springs district temperatures of 41°C. Both of these simulations required highly permeable crystalline basement rocks (10^{-13} and 10^{-12} m^2). Increasing or decreasing basement permeabilites beyond this range resulted in reduced temperatures in the hot-springs district.

tinuous. This hydrologic window allows waters circulating deep within the crystalline basement to ascend relatively rapidly and discharge in the hot-springs district.

Two-dimensional hydrothermal modeling does not support a shallow groundwater circulation hypothesis in which flow is primarily confined to the Magdalena Group carbonates, as argued by most previous studies. In this scenario, convective heat transport was negligible and observed hot-springs district temperatures could not be reproduced. Allowing groundwater to circulate deeply within the system through permeable crystalline basement rocks and ascend directly under the hot-springs district best-matched observations. Consequently, we conclude that groundwater circulation to depths ranging from 2 to 8 km within fractured crystalline basement rocks of effective permeability on the order of 10^{-12} m^2 is required to account for the geothermal anomaly. Although geothermal water is transmitted to the surface through a carbonate aquifer, our results indicate that the geothermal water enters the carbonate aquifer from the fractured crystalline basement at relatively shallow depths and that the carbonate aquifer is not the route for long-distance flow.

Our hydrothermal model was able to reproduce the temperature range of measured temperature profiles, but not their shallow curvature patterns. The temperature curvature typically takes place in the upper 10 m of the subsurface (Fig. 6). Capturing this level of detail would require a more refined finite element mesh not practical for our regional scale application. To some degree, these shallow, cooler temperatures may be the result of transient hydrologic conditions during periods of time when the Rio Grande river stage is higher than the alluvial aquifer. Our models were quasi-steady-state. Down valley transport of cool water coming into the hot-springs district perpendicular to our cross-sectional model may also explain, in part, this curvature in the shallow temperature profiles. The warmest hot-springs district temperatures in our model results are about 300 m south of where observed hottest temperatures were measured in the hot-springs district. This discrepancy may simply be the result of focusing on a localized area of a regional model; it is also possible that lithologic heterogeneities or faults not represented in our model are influencing local geothermal water flow. For example, south-dipping faults may be acting as conduits. In our simulations, faults are not modeled as conduits or barriers and would therefore fail to capture this effect. Considering the regional scale of our modeling effort, these localized divergences are not unexpected.

There remains some nonuniqueness in our model results due to parameter uncertainty. Like many other studies, we found that permeability had the largest effect on model results (e.g., Smith & Chapman 1983). This is why our calibration procedure focused on varying permeability. However, other parameters such as porosity can also have some effect on model results. Due to lack of data, it was necessary to assume average representative porosities for lithologies in our model consistent with Freeze & Cherry (1979). To assess the implications of this assumption, we re-ran one of our deep-circulation scenarios (basement permeability 10^{-13} m^2) but doubled the porosity of the modeled crystalline basement rocks to 0.10. This increased simulated hot-springs district temperatures by 0.8%, groundwater ages by 3.8%, and maximum reservoir temperatures by 2.2% and decreased average specific discharge by 0.2%. Groundwater

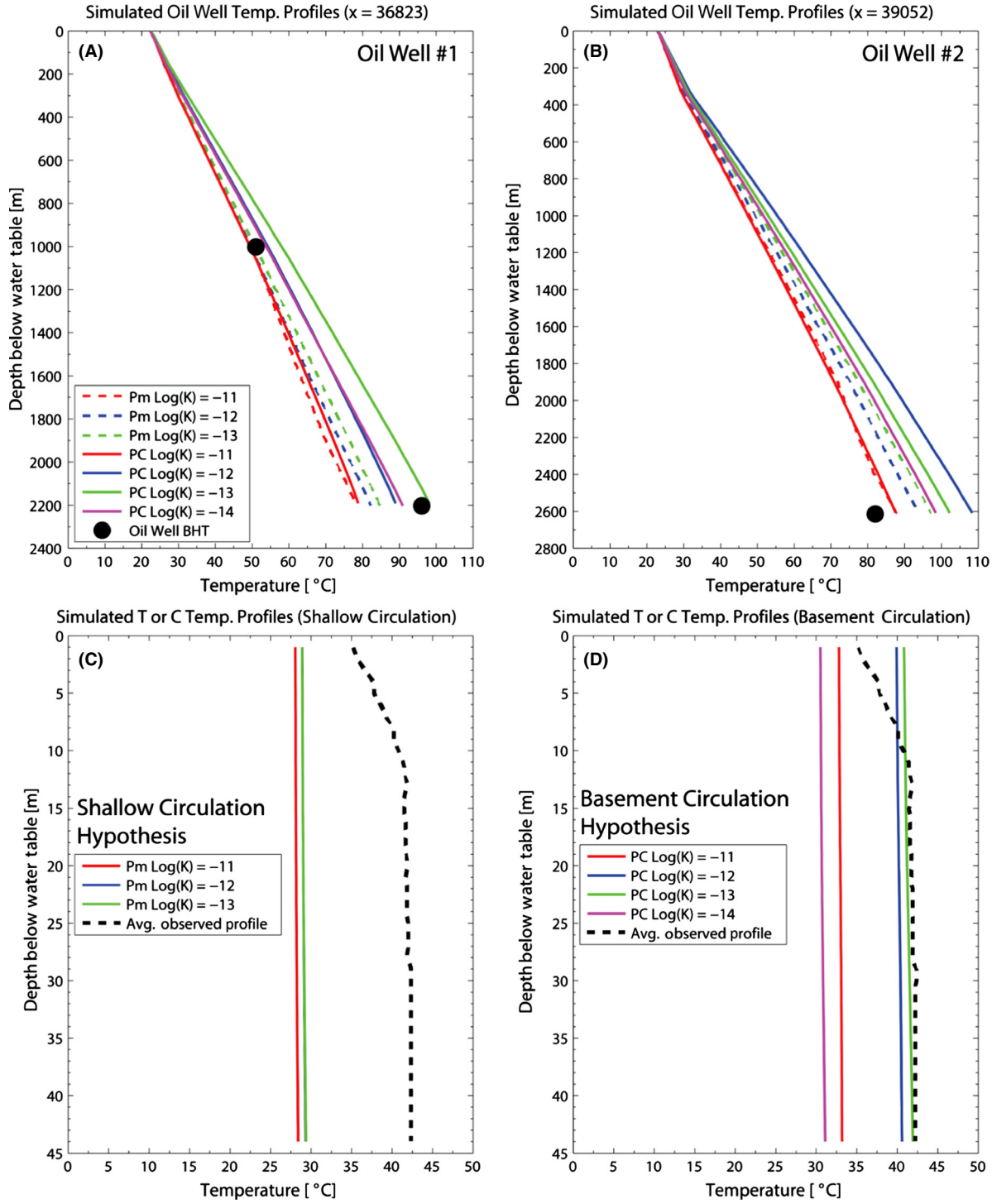

Fig. 13. Comparison of simulated and observed temperatures along the model domain. The assigned base-10 logarithm permeabilities for the crystalline basement rocks (PC) and Magdalena Group (Pm) are shown in the legends (graphs A and B share the same legend). Simulated temperature profiles are compared to bottom-hole temperature data collected in oil wells approximately 15 km north of Truth or Consequences (Top, A and B). They agree fairly well with bottom-hole temperature data, suggesting our assigned thermal properties, such as basal heat flux and thermal conductivites, represent those of the study area. Average simulated and measured temperature profiles from the hot-springs district are compared in C and D. Only simulations having high crystalline basement permeability (10^{-13} and 10^{-12} m^2) were able to reproduce observed hot-springs district temperatures.

age was most sensitive to changes in porosity. However, increasing crystalline basement porosity by 100% led to changes in all parameters of <4%, some <1%. This nonlinear relationship to porosity is due to the coupled nature of fluid flow and heat transport. Doubling porosity in our model decreased seepage velocities, but not by a factor of two. It also resulted in a lower bulk thermal conductivity and a slight temperature increase. However, this temperature increase was accompanied by a decrease in viscosity, which increased seepage velocities and partially compensated for changing porosity. This led us to conclude that the model sensitivity to porosity is small relative to permeability.

Geochemistry results also support the basement-circulation hypothesis. The Na^+/Cl^--dominated composition of typical hot-springs district geothermal waters is characteristic of geothermal water derived from igneous and metamorphic rocks (Kühn 2004; Stober & Bucher 2007; Bucher & Stober 2010). In addition, the spatial distribution of water composition and the co-variation of several geothermally associated parameters suggest that geothermal waters mix with shallow groundwater. The distinct chemical differences between Italian carbonate-reservoir geothermal waters and the Truth or Consequences waters are strong evidence against long-term residence in carbonate rocks in our study area (Chiodini *et al.* 1995). In contrast, the chemistry of geothermal waters from the Socorro, New Mexico, and the Truth or Consequences hot-springs district is nearly identical (Owens 2013). Studies investigating groundwater flow patterns of the Socorro geothermal system have found its geothermal anomaly is likely the result of deep groundwater circulation within crystalline basement rocks (Barroll & Reiter 1990; Mailloux *et al.* 1999), thus supporting the basement-circulation hypothesis for Truth or Consequences.

We hypothesize that the geothermal waters enter the system in the Sierra Cuchillo and San Mateo Mountains and flow downward until they contact crystalline basement rocks. High permeability enables the water to move through, and geochemically react with, the granitic/metamorphic rocks at relatively high temperatures (probably >150°C) for thousands of years at depths ranging from 2 to 8 km. Geothermometry indicates maximum geothermal reservoir temperatures around 170°C. This suggests geothermal groundwater circulation is focused toward the shallower end of the 2 to 8 km depth range (around 4 km assuming a temperature gradient of 40°C km^{-1}; Reiter *et al.* 1986). The rock/water chemical reactions in this environment produce a characteristic geothermal Na^+/Cl^- composition. The geothermal waters eventually ascend under the hot-springs district where a hydrologic window exists due to the absence of overlying confining units. In transit toward the shallow Quaternary alluvial sediments in which most hot-springs district wells are currently completed, the waters traverse a Paleozoic limestone unit and in some instances mix with shallow groundwater. The geothermal water moves through the limestone rapidly enough that it does not have time to re-equilibrate with the carbonate rocks. Once in the shallow alluvial aquifer, geothermal waters flow laterally until they discharge to the Rio Grande or are extracted by wells.

This study provides additional evidence that the crystalline basement rocks beneath the Rio Grande Rift can be remarkably permeable. Mailloux *et al.* (1999) and Barroll & Reiter (1990) studied the Socorro geothermal system located approximately 115 km north of Truth or Consequences and estimated crystalline basement permeability of 10^{-14} m^2 (Mailloux *et al.* 1999). Figure 1 compares these Rio Grande Rift permeabilities to the crustal permeability trends determined by previous studies. Permeabilities within the Rio Grande Rift are high in comparison. This suggests that large fault structures and significant fracture networks have substantially increased the permeability of the crystalline basement, potentially during the Laramide orogeny or due to the ongoing extension of the rift.

It is noteworthy that we were able to reproduce temperature anomalies in the hot-springs district when using a constant permeability-with-depth modeling scheme for each lithology. This is consistent with the results of Burns *et al.* (2014) in this *Geofluids* special issue. Burns *et al.* (2014) tested additional schemes involving step-function permeability transitions at depth based on available well data. The results from both step-function and constant permeability schemes were similar in that they reasonably reproduced observed temperature anomalies. Like Burns *et al.* (2014), our modeling results indicated that allowing permeability to decay with depth in accordance with the Manning & Ingebritsen (1999) power law lead to conduction-dominated heat transfer, due to the rapid decline of permeability. A constant permeability scheme for regional hydrologic models of this scale appears to be a reasonable simplification, and the resulting permeabilities should be interpreted as effective regional permeabilities.

Future modeling efforts within continental rifts should consider the possibility of highly permeable crystalline basement rocks that promote deep circulation of groundwater, in conjunction with hydrologic windows in confining units, as key factors in the generation of low-temperature geothermal systems. Modeling efforts that capture the three-dimensional geometry of systems could better interrogate the effects of water-table configuration and geologic heterogeneity. The possibility that discrete high-permeability faults serve as conduits for geothermal waters also warrants consideration.

ACKNOWLEDGEMENTS

We would like to extend our gratitude to the City of Truth or Consequences and its residents for their assistance and cooperation throughout our study. This research was funded by the City of Truth or Consequences, New Mexico Bureau of Geology and Mineral Resources (Aquifer

Mapping Program), Department of Energy award DE-EE0002850 (funded part of the temperature logging effort), and the National Science Foundation (EPSCoR) under Grant No. IIA-1301346.

REFERENCES

Anderholm SK (2001) Mountain-front recharge along the east side of the Albuquerque Basin, Central New Mexico. *U.S. Geological Survey Water-Resour. Invest. Rep. 00-4010.* 36 pp.

Arehart GB, Coolbaugh MF, Poulson SR (2003) Evidence for a magmatic source of heat for the Steamboat Springs geothermal system using trace elements and gas geochemistry. *Geothermal Resources Council Transactions*, **27**, 269–74.

Baldridge WS, Keller GR, Haak V, Wendlandt E, Jiracek GR, Olsen KH (1995) The Rio Grande Rift. In: *Continental Rifts: Evolution, Structure, Tectonics* (ed. Olsen KH), Elsevier, Amsterdam. *Developments in Geotectonics*, **25**, 233–65.

Barroll MW, Reiter M (1990) Analysis of the Socorro hydrogeothermal system: Central New Mexico. *Journal of Geophysical Research*, **95**, 21949–63.

Batzle M, Wang Z (1992) Seismic properties of pore fluids. *Geophysics*, **57**, 1396–408.

Bredehoeft JD, Papadopulos IS (1965) Rates of vertical groundwater flow estimated from the Earth's thermal profile. *Water Resources Research*, **1**, 325–8.

Bucher K, Stober I (2010) Fluids in the upper continental crust. *Geofluids*, **10**, 241–53.

Burns ER, Williams CF, Ingebritsen SE, Voss CI, Spane FA (2014) Understanding heat and groundwater flow through the Columbia Plateau regional aquifer system: insights gained from alternative models of permeability/depth relationships. *Geofluids*, **15**, 120–38.

Chiodini G, Frondini F, Marini L (1995) Theoretical geothermometers and PCO2 indicators for aqueous solutions coming from hydrothermal systems of medium-low temperature hosted in carbonate-evaporite rocks. Application to the thermal springs of the Etruscan Swell, Italy. *Applied Geochemistry*, **10**, 337–46.

Dingman SL (2002) *Physical hydrology*, 2nd edn. Waveland Press, Long Grove, IL, 656 p.

Dunbar N (2005) Quaternary volcanism in New Mexico. *New Mexico Museum of Natural History and Science Bulletin*, **28**, 95–106.

Ellis AJ, Mahon WAJ (1964) Natural hydrothermal systems and experimental hot water/rock interactions. *Geochimica et Cosmochimica Acta*, **28**, 1323–57.

Ellis AJ, Mahon WAJ (1967) Natural hydrothermal systems and experimental hot water/rock interactions (Part II). *Geochimica et Cosmochimica Acta*, **31**, 519–38.

Ferguson CA, Osburn GR, McIntosh WC (2012) Oligocene calderas in the San Mateo Mountains, Mogollon-Datil volcanic field, New Mexico. *New Mexico Geological Society Guidebook*, **63**, 74–7.

Fournier RO (1979) A revised equation for the Na/K geothermometer. *Geothermal Resources Council Transactions*, **3**, 221–4.

Fournier RO (1981) Application of water geochemistry to geothermal exploration and reservoir engineering In: *Geothermal Systems: Principles and Case Histories* (eds Ryback L, Muffler LJP), pp. 109–43. John Wiley and Sons, NY.

Fournier R (1989) Lectures on geochemical interpretation of hydrothermal waters. *UNU Geothermal Training Programme, Reykjavik Iceland*, 10, 54 p.

Fournier RO, Potter RW II (1982) A revised and expanded (quartz) geothermometer. *Geothermal Resources Council Bulletin*, **11**, 3–12.

Freeze RA, Cherry JA (1979) *Groundwater*. Prentice Hall, Englewood Cliffs, NJ, USA 604 p.

Fritz DE, Farmer GL, Verplanck EP (2006) Application of Sr isotopes in secondary silicate minerals to paleogroundwater hydrology: an example from K-metasomatized rocks in the western US. *Chemical Geology*, **235**, 276–85.

Furlong KP, Hanson RB, Bowers JR (1991) Modeling thermal regimes. *Reviews in Mineralogy*, **26**, 437–505.

Gerdes M, Baumgartner L, Person M (1995) Permeability heterogeneity in metamorphic rocks: implications from stochastic modeling. *Geology*, **23**, 945–8.

Giggenbach WF (1986) Graphical techniques for the evaluation of water/rock equilibrium conditions by use of Na, K, Mg and Ca contents of discharge waters. *Proceedings of the Eighth New Zealand Geothermal Workshop*, Auckland, New Zealand, 37–43.

Giggenbach WF (1988) Geothermal solute equilibria. Derivation of Na-K-Mg-Ca geoindicators. *Geochimica Cosmochimica Acta*, **52**, 2749–65.

Giggenbach W (1991) Chemical techniques in geothermal exploration. *UNITAR/UNDP Guidebook: Application of geochemistry in resources development*, 119–44.

Gilmer A, Mauldin R, Keller G (1986) A gravity study of the Jornado Del Muerto and Palomas Basins. *New Mexico Geological Society Guidebook*, **37**, 131–4.

Gleeson T, Smith L, Moosdorf N, Hartmann J, Dürr H, Manning A, Beek L, Jellinek A (2011) Mapping permeability over the surface of the Earth. *Geophysical Research Letters*, **38**, L02401, 6p.

Harder H (1959) Contribution to the geochemistry of boron: part II: boron in sediments. *Nachr. Akad. Wiss. Göttingen: II. Math.-Physik. K1.*, **6**, 123–83.

Harrison R, Cather S (2004) The Hot Springs fault systems of south-central New Mexico—evidence for northward translation of the Colorado Plateau during the Laramide orogeny. *New Mexico Bureau of Geology and Mineral Resources, Bulletin*, **160**, 161–80.

Harrison R, Lozinsky R, Eggleston T, McIntosh W (1993) Geologic map of the Truth or Consequences 30x60 minute quadrangle. *New Mexico Bureau of Mines and Mineral Resources Open-file Report 390*, Socorro, 1:100,000 scale, 1 sheet, 16 p.

Ingebritsen SE, Manning CE (1999) Geological implications of a permeability-depth curve for the continental crust. *Geology*, **27**, 1107–10.

Ingebritsen SE, Manning CE (2010) Permeability of the continental crust: dynamic variations inferred from seismicity and metamorphism. *Geofluids*, **10**, 193–205.

Karingithi C (2009) Chemical geothermometers for geothermal exploration. *Short Course IV on Exploration for Geothermal Resources, organized by UNU-GTP, KenGen and GDC*, 12 p.

Kelley SA, Chapin CE (1997) Cooling histories of mountain ranges in the southern Rio Grande Rift based on apatite fission-track analysis – a reconnaissance survey. *New Mexico Geology*, **19**, 1–14.

Kühn M (2004) *Reactive Flow Modeling of Hydrothermal Systems.* Springer Berlin Heidelberg, New York, NY, 264 p.

Lozinsky RP (1987) Cross-section across the Jornado del Muerto, Engle, and Northern Palomas Basins, south-central New Mexico. *New Mexico Geology*, **9**, 55–7.

Mailloux B, Person M, Kelley S, Dunbar N, Cather S, Strayer L, Hudleston P (1999) Tectonic controls on the hydrogeology of

the Rio Grande Rift, New Mexico. *Water Resources Research*, **35**, 2641–59.
Manning CE, Ingebritsen SE (1999) Permeability of the continental crust: the implications of geothermal data and metamorphic systems. *Reviews of Geophysics*, **37**, 127–50.
Morgan P, Seager WR, Golombek MP (1986) Cenozoic thermal mechanical and tectonic evolution of the Rio Grande Rift. *Journal of Geophysical Research*, **91**, 6263–76.
Owens L (2013) Geochemical investigation of hydrothermal and volcanic systems in Iceland, New Mexico and Antarctica. *Doctoral Thesis, New Mexico Institute of Mining and Technology*, 300 p. http://www.ees.nmt.edu/outside/alumni/papers/2013d_owens_lb.pdf
Person M, Taylor J, Dingman S (1998) Sharp interface models of salt water intrusion and wellhead delineation on Nantucket Island, Massachusetts. *Groundwater*, **36**, 731–42.
Person M, Banerjee A, Hofstra D, Sweetkind D, Gao Y (2008) Hydrologic models of modern and fossil geothermal systems within the Great Basin: implications for Carlin-Type gold mineralization. *Geosphere*, **4**, 888–917.
Plummer LN, Bexfield LM, Anderholm SK, Sanford WE, Eurybiades B (2004) Geochemical characterization of groundwater flow in the Sante Fe Group aquifer system, Middle Rio Grande Basin, New Mexico. *U.S. Geological Survey Water-Resources Investigations Report*, 03-4131, 395 p.
Powell WC (1929) Report of an investigation of the Hot Springs Artesian Basin, Hot Springs, New Mexico. *Ninth Biennial Report of the State Engineer of New Mexico*, 1929–1930, 120–9.
Powell T, Cumming W (2010) Spreadsheets for geothermal water and gas geochemistry. *Proceedings of the 35th Workshop on Geothermal Reservoir Engineering, Stanford University*, SGP-TR-188, 10 p.
Raffensperger JP, Garven G (1995) The formation of unconformity-type uranium ore deposits; 1, Coupled groundwater flow and heat transport modeling. *American Journal of Science*, **295**, 581–636.
Reiter M, Eggleston R, Broadwell B, Minier J (1986) Estimates of terrestrial heat flow from deep petroleum tests along the Rio Grande Rift in Central and Southern New Mexico. *Journal of Geophysical Research*, **91**, 6225–45.
Rojstaczer SA, Wolf S (1992) Permeability changes associated with large earthquakes: an example from Loma Prieta, California. *Geology*, **20**, 211–4.
Sanford RM, Bowers RL, Combs J (1979) Rio Grande Rift geothermal exploration case history, Elephant Butte prospect, south-central New Mexico. *Transactions, Geothermal Resources Council*, **3**, 609–12.
Sass JH, Lachenbruch AH, Munroe RJ, Green GW, Moses TH Jr (1971) Heat flow in the western United States. *Journal of Geophysical Research*, **76**, 6356–431.
Seager WR, Mack GH (2003) Geology of the Caballo Mountains, New Mexico. *New Mexico Bureau of Geology and Mineral Resources Memoir*, **49**, 136.
Seager WR, Morgan P (1979) Rio Grande Rift in southern New Mexico, west Texas, and northern Chihuahua. In: *Rio Grande Rift-Tectonics and Magmatism* (ed. Riecker RE), 87–106. American Geophysical Union, Washington, DC, USA.
Senger RK, Fogg GE (1990) Stream functions and equivalent freshwater heads for modeling regional flow of variable-density ground water; 2, application and implications for modeling strategy. *Water Resources Research*, **26**, 2097–106.
Shmonov VM, Vitiovtova VM, Zharikov AV, Grafchikov AA (2003) Permeability of the continental crust: implications of experimental data. *Journal of Geochemical Exploration*, **78–79**, 697–9.
Smith L, Chapman DS (1983) On the thermal effects of groundwater flow: 1. Regional scale systems. *Journal of Geophysical Research*, **88**, 593–608.
Stober I, Bucher K (2007) Hydraulic properties of the crystalline basement. *Hydrogeology Journal*, **15**, 213–24.
Summers WK (1976) Catalog of Thermal Waters in New Mexico. *New Mexico Bureau of Mines and Mineral Resources Hydrologic Report*, 4, 80 p.
Theis CV (1963) Estimating the transmissivity of a water-table aquifer from the specific capacity of a well. *U.S. Geological Survey Water Supply Paper*, 1536-I, 332–6.
Theis CV, Taylor GC, Murray CR (1941) Thermal waters of the Hot Springs Artesian Basin, Sierra County, NM. *Fourteenth and Fifteenth Biennial Reports of the State Engineer of New Mexico*, 1938–1942, 421–92.
Walker CT (1975) Geochemistry of boron. *Benchmark Papers in Geology*, 23, 423 pp.
Weissmann GS, Zhang Y, LaBolle EM, Fogg GE (2002) Dispersion of groundwater age in an alluvial aquifer system. *Water Resources Research*, **38**, 1198.
Wells SG, Granzow H (1981) Hydrogeology of the thermal aquifer near Truth or Consequences, New Mexico. In: State-Coupled Low-Temperature Geothermal Resource Assessment Program, Fiscal Year 1980, 3-5 to 3-51.
Witcher JC (1988) Geothermal resources of southwestern New Mexico and southeastern Arizona. *New Mexico Geological Society Guidebook*, **39**, 191–8.
Ziagos JP, Blackwell DD (1986) A model for the transient temperature effects of horizontal fluid flow in geothermal systems. *Journal of Volcanology and Geothermal Research*, **27**, 371–97.

APPENDIX A

Well Inventory, including denotion of the analyses and graphics they were utilized for

ID #	UTM X	UTM Y	Type	Depth [m]	Piper	Chem. Mixing	Temp. Profile	Geothermometry	Carbon-14
TC-12	289524	3667924	Pump	34	x	x		x	x
TC-13	289772	3667577	Artesian	53	x	x	x	x	x
TC-18	289651	3667673	Pump	12	x	x		x	
TC-19	289627	3667745	Open	12			x		
TC-20	289609	3667730	Open	12			x		
TC-21	289439	3667679	Open	12			x		
TC-35	289398	3667845	Pump	63	x	x	x	x	
TC-37	290053	3667623	Open	17			x		
TC-38	289989	3667658	Open	18			x		
TC-46	289889	3667656	Open	14			x		
TC-48	289951	3667745	Open	12			x		
TC-51	290048	3667712	Open	15			x		
TC-56	289558	3667652	Pump	44			x		
TC-59	289688	3667756	Open	15	x	x	x	x	x
TC-61	289996	3667633	Open	22	x	x	x	x	x
TC-62	288638	3679885	Pump	183					x
TC-63	289775	3667472	Pump	30	x	x	x	x	
TC-64	290436	3671828	Pump	30	x	x			
TC-65	290782	3671749	Pump	61	x	x			
TC-72	289530	3667647	Pump	67			x		
TC-76	289253	3667755	Pump	65	x	x		x	x
TC-82	289528	3667839	Pump	32		x			
TC-94	289765	3667869	Pump	8	x	x		x	
TC-97	289977	3667846	Pump	30		x			
TC-98	289863	3667626	Artesian	56	x	x		x	
TC-100	290458	3668222	Artesian	37	x	x			
TC-101	289756	3667667	Pump	4	x	x		x	
TC-114	290016	3667630	Open	74			x		
TC-505	289825	3667969	Spring	–	x	x		x	
TC-508	289602	3667919	Spring	–	x	x		x	
Datum: NAD83, UTM Zone 13				Count	16	18	16	13	6

APPENDIX B

Chemical analyses_ from this study

Parameter	D. Limit	Units	TC-12	TC-13	TC-18	TC-35	TC-59	TC-61	TC-62	TC-63	TC-64	TC-65	TC-76
Date Collected		-	1/9/2013	9/5/2013	1/9/2013	1/8/2013	1/8/2013	1/8/2013	1/8/2013	1/8/2013	1/8/2013	1/8/2013	9/5/2013
Alkalinity as $CaCO_3$	5	mg L^{-1}	176	173	175	173	177	181	111	182	137	23	173
Aluminum	0.0005	mg L^{-1}	ND	ND	ND	ND	ND	ND	0.0035	ND	ND	0.006	ND
Anions total		meq L^{-1}	44.28	44.67	43.88	43.77	42.56	43.66	23.86	43.2	16.18	43.87	45.05
Antimony 121	0.0005	mg L^{-1}	ND	ND	ND	ND	ND	ND	ND	ND	ND	ND	ND
Arsenic	0.0005	mg L^{-1}	ND	ND	ND	ND	ND	ND	0.0025	ND	ND	ND	ND
Barium	0.001	mg L^{-1}	0.197	0.190	0.206	0.216	0.206	0.182	0.197	0.170	0.102	0.017	0.197
Beryllium	0.0005	mg L^{-1}	ND	ND	ND	ND	ND	ND	ND	ND	ND	ND	ND
Bicarbonate (HCO_3)	5	mg L^{-1}	215	211	214	211	216	221	136	222	168	28	211
Boron 11	0.005	mg L^{-1}	0.345	0.303	0.340	0.345	0.354	0.342	0.203	0.394	0.194	1.220	0.296
Bromide	0.01	mg L^{-1}	0.126	ND	0.134	0.122	0.129	0.180	ND	0.121	0.041	0.210	ND
Cadmium 111	0.0005	mg L^{-1}	ND	ND	ND	ND	ND	ND	ND	ND	ND	ND	ND
Calcium	0.05	mg L^{-1}	163	165	160	160	157	163	139	140	128	246	164
C13/C12 Ratio		-	−21.1	−19.8			−10.0	−18.5	−17.3				−21.3
Carbon-14		years	5490	6870			11480	7110	4040				5510
Carbon-14 Fraction		fmdn	−0.211	−0.198			−0.100	−0.185	−0.173				−0.213
Carbonate (CO_3)	5	mg L^{-1}	ND	ND	ND	ND	ND	ND	ND	ND	ND	ND	ND
Cations total		meq L^{-1}	43.85	43.07	43.41	44.11	42.37	42.87	23.55	41.81	15.80	41.79	42.92
Chloride	1	mg L^{-1}	1370	1390	1360	1370	1290	1350	720	1330	380	784	1410
Chromium	0.0005	mg L^{-1}	ND	ND	ND	ND	ND	ND	0.0033	ND	0.0031	ND	ND
Cobalt	0.0005	mg L^{-1}	ND	ND	ND	ND	ND	ND	ND	ND	ND	ND	ND
Copper 65	0.0005	mg L^{-1}	0.0069	0.0062	ND	ND	ND	ND	0.0081	ND	ND	0.0093	0.0520
Fluoride	0.1	mg L^{-1}	3.10	3.14	3.11	3.12	3.18	3.09	2.87	3.42	1.43	4.26	3.37
Hardness ($CaCO_3$)		mg L^{-1}	483	479	474	474	479	482	382	411	380	667	477
Iron	0.02	mg L^{-1}	ND	ND	ND	ND	0.611	ND	ND	ND	ND	ND	ND
Lead	0.0005	mg L^{-1}	ND	ND	ND	ND	ND	0.0053	ND	ND	ND	ND	ND
Lithium	0.001	mg L^{-1}	1.140	1.200	1.150	1.170	1.110	1.160	0.482	1.120	0.158	0.526	1.190
Magnesium	0.05	mg L^{-1}	18.3	16.7	18.3	18.0	21.2	18.4	8.4	14.8	14.9	13.1	16.4
Manganese	0.001	mg L^{-1}	ND	ND	ND	ND	0.034	ND	ND	ND	ND	0.057	0.016
Molybdenum 95	0.001	mg L^{-1}	ND	ND	ND	ND	ND	ND	ND	ND	ND	0.032	ND
Nickel	0.0005	mg L^{-1}	ND	ND	ND	ND	ND	ND	0.0045	ND	0.0053	0.0092	0.0059
Nitrate	0.1	mg L^{-1}	2.71	2.40	2.34	2.35	2.04	2.40	1.35	1.86	1.81	ND	2.49
Nitrite	0.1	mg L^{-1}	ND	ND	ND	ND	ND	ND	ND	ND	ND	ND	ND
Ortho Phosphate	0.5	mg L^{-1}	ND	ND	ND	ND	ND	ND	ND	ND	ND	ND	ND
Percent difference		%	−0.48	−1.83	−0.55	0.38	−0.23	−0.91	−0.64	−1.64	−1.19	−2.43	−2.42
pH		ph Units	7.3	7.1	7.4	7.2	7.2	7.1	7.5	7.2	7.6	8.0	7.6
Potassium	0.05	mg L^{-1}	57.80	56.00	56.60	58.60	55.20	55.50	13.10	65.60	7.17	11.60	56.20
Selenium	0.001	mg L^{-1}	ND	ND	ND	ND	ND	ND	ND	ND	ND	ND	ND
Silicon	0.02	mg L^{-1}	20.3	22.2	20.3	20.7	19.0	20.9	32.0	25.9	15.1	5.8	21.4
Silver 107	0.0005	mg L^{-1}	ND	ND	ND	ND	ND	ND	ND	ND	ND	ND	ND
SiO_2	0.05	mg L^{-1}	43.4	47.5	43.5	44.2	40.6	44.6	68.5	55.4	32.3	12.5	45.8
Sodium	0.05	mg L^{-1}	752	737	747	762	721	731	358	734	184	647	734
Specific Conductance		uS cm^{-1}	4680	4660	4650	4650	4560	4650	2570	4530	1710	4170	4700
Strontium	0.001	mg L^{-1}	3.96	3.89	3.90	3.96	4.03	3.92	2.48	3.47	1.56	8.48	3.90
Sulfate	1	mg L^{-1}	85.2	80.2	81.8	75.2	112.0	87.5	54.3	85.9	125.0	1010.0	77.6

Appendix B. (Continued)

Parameter	D. Limit	Units	TC-12	TC-13	TC-18	TC-35	TC-59	TC-61	TC-62	TC-63	TC-64	TC-65	TC-76
TDS calc		mg L^{-1}	2610	2610	2590	2600	2520	2570	1440	2550	961	2750	2620
Field Temperature		°C	40.85	42.70	43.09	44.80	44.10	41.20	26.62	40.12	21.83	19.77	46.10
Thallium	0.0005	mg L^{-1}	ND	ND	ND	ND	ND	ND	ND	ND	ND	ND	ND
Thorium	0.0005	mg L^{-1}	ND	ND	ND	ND	ND	ND	ND	ND	ND	ND	ND
Tin	0.0005	mg L^{-1}	ND	ND	ND	ND	ND	ND	ND	ND	ND	ND	ND
Titanium	0.001	mg L^{-1}	ND	ND	ND	ND	ND	ND	0.006	ND	ND	ND	ND
Tritium		mg L^{-1}					0.10	0.18	−0.02				
Uranium	0.0005	mg L^{-1}	ND	ND	ND	ND	ND	ND	0.0076	ND	ND	ND	ND
Vanadium	0.0005	mg L^{-1}	0.0083	0.0101	0.0088	0.0090	ND	0.0089	0.0077	0.0111	0.0066	ND	0.0079
Zinc 66	0.0005	mg L^{-1}	0.0139	ND	0.0093	ND	ND	0.0068	0.0062	ND	ND	0.0168	0.0351

